Noname manuscript No.
(will be inserted by the editor)

Lattice Boltzmann Methods for global linear instability analysis

José Miguel Pérez · Alfonso Aguilar · Vassilis Theofilis

Received: date / Accepted: date

Abstract Modal global linear instability analysis is performed using, for the first time ever, the Lattice Boltzmann Method (LBM) to analyze incompressible flows with two and three inhomogeneous spatial directions. Four linearization models have been implemented in order to recover the linearized Navier-Stokes equations in the incompressible limit. Two of those models employ the single relaxation time and have been proposed previously in the literature as linearization of the collision operator of the lattice Boltzmann equation. Two additional models are derived herein for the first time by linearizing the local equilibrium probability distribution function.

Instability analysis results are obtained in three benchmark problems, two in closed geometries and one in open flow, namely the square and cubic lid-driven cavity flow and flow in the wake of the circular cylinder. Comparisons with results delivered by classic spectral-element methods verifies the accuracy of the proposed new methodologies and points potential limitations particular to the LBM approach. The known issue of appearance of numerical instabilities when the SRT model is used in direct numerical simulations employing the LBM, is shown to be reflected in a spurious global eigenmode when the SRT model is used in the instability analysis. Although this mode is absent in the multiple relaxation times model, other spurious instabilities can also arise and are documented herein. Areas of potential improvements in order to make the proposed methodology competitive with established approaches for global instability analysis are discussed.

Keywords Lattice Boltzmann methods · complex geometries · global instability analysis · flow control

1 Introduction

A major element in obtaining a numerical solution of the equations of motion involves meshing the geometry in question, while in incompressible flow pressure must be treated appropriately in order to ensure divergence free solutions. Both of these aspects are inherently linked to the constant growth in popularity of the lattice Boltzmann method (LBM), which is capable of addressing flows in complex geometries meshed in a simple manner, besides not requiring the solution of a pressure Poisson equation

José Miguel Pérez
School of Aeronautics, Universidad Politécnica de Madrid, Spain
Tel.: +34 91 336 32 98
E-mail: josemiguel.perez@eupm.es

Alfonso Aguilar
School of Aerospace, Transport and Manufacturing, Cranfield University. UK

Vassilis Theofilis
The University of Liverpool, School of Engineering, The Quadrangle, Brownlow Hill, Liverpool, L69 3GH, UK
Also at: Theoretical and Applied Mechanics Laboratory, Department of Mechanical Engineering, Universidade Federal Fluminense, Rua Passo da Patria 156, Niterói, RJ 24210-240, Brazil

and being easily parallelizable. Unlike classic Computational Fluid Dynamics (CFD) methods which solve a set of partial differential equations on a pre-defined mesh, the LBM is based on predicting the dynamics of a number of particles which mimic fluid flow at the mesoscale level. The link with the incompressible Navier-Stokes equations of motion is provided by expanding the lattice Boltzmann equation using Taylor series in time and space and making the Chapman-Énskog multiscale expansion [15]. This expression is only valid when density variations are small over the entire domain [38,47], i.e. when the Mach number and pressure variations are order $O(\epsilon)$ and $O(\epsilon^2)$, respectively, ϵ being the Knudsen number. Then the Maxwell distribution function is expanded, assuming a low-order Mach number approximation which is a quadratic velocity function responsible for the non-linear terms. An important simplification of the LBM was made by Higuera and Succi [28] and Higuera and Jiménez [27] who proposed a linear and stable collision operator in the limit $\epsilon \ll 1$. The collision operator changes the probability distribution function (PDF) towards an equilibrium function, the moments of which match the low Mach number Maxwell-Boltzmann distribution function. The evolution of the probability distribution function using a single relaxation time is given the lattice Boltzmann equation[1], LBE,

$$\frac{\partial f_\alpha}{\partial t} + \mathbf{e}_\alpha \cdot \nabla f_\alpha = -\frac{1}{\tau}\left(f_\alpha - f_\alpha^{eq}\right) , \tag{1}$$

where f_α and f_α^{eq} respectively denote the non-equilibrium and equilibrium PDF for a given velocity $\mathbf{e}_\alpha$, and τ is the collision relaxation time. The PDF represents the probability of finding a particle with a velocity $\mathbf{e}$ at a location $\mathbf{x}$ at a time t while the equation is discretized in the lattice space (Cartesian grid with equidistant lattice molecules). The right hand side of equation (1) represents the collision operator when the Bhatnagar − Gross − Krook scheme, BGK, is considered [43], implying the use of a single dimensionless collision relaxation time, SRT for short. The operator is constructed in discrete velocity space and is isotropic, while τ is related with the macroscopic kinematic viscosity. The multi-relaxation time (MRT) model [18,19] is based on the generalized LBE and considers additional relaxation times, chosen in order to remove non-hydrodynamic modes which were seen to be introduced on the grid scale by the SRT model and lead to instabilities in the simulations [46]. The MRT approach is constructed in moment- rather than in discrete velocity space but, despite its advantage over SRT, it could not altogether eliminate diverging solutions in the incompressible limit. Finally, several compressible versions of the LBM have appeared in the literature, see, e.g. [3,37,42, 17].

On the other hand, it has long been established [23,41,33,13] that one of the most stringent tests that can be applied in order to assess the quality of a numerical method for the solution of the fluid flow equations of motion in a direct numerical simulation context, is to reproduce linear instability analysis results by a DNS code. Dispersion and dissipation errors can be assessed through the degree of accuracy by which frequencies and amplification/damping rates of linear eigenmodes are reproduced by any given DNS scheme. This, of course, holds true for the LBM approach too where, to the authors' knowledge, to-date no systematic demonstration exists on the reproduction of linear stability theory results by an LBM DNS code. Furthermore, if an LBM approach is to be used in order to reliably predict flow (and acoustic) instabilities in complex geometries, it is worthwhile posing the above question in the framework of global linear instability [49].

Efforts related with instability analysis have appeared in the LBM literature. One of the first works dealing with the stability of LBM schemes by Benzi et al. [5] assumed a linearized collision operator that neglects nonlinear terms. From a physical point of view, this assumption corresponds to the rather uninteresting case of imposing a basic flow that is either zero or uniform in space. Lallemand and Luo [34] and Bouzidi *et al.* [10] employed von Neumann stability analysis and imposed desirable physical and mathematical properties of the solution, such as isotropy of the transport coefficients and Galilean invariance of wave propagation, in order to fix the relaxation times used by the MRT model and showed that the latter is numerically more stable that its SRT counterpart. In addition, they proved that the numerical stability of LBM is affected significantly by the local grid structure. Niu *et al.* [39] also performed von Neumann stability analysis assuming a uniform base flow. Their analysis showed that the lattice Boltzmann equation with interpolations, such as the differential

[1] Usually called LBGK model

lattice Boltzmann equation, improves the numerical stability of the LBM. Moreover, the expression of the Jacobian that appears in the linearization of the lattice Boltzmann equation is presented for the first time by these authors. In fact, numerical stability criteria applied to the lattice Boltzmann equation with SRT advise use of $\tau = 2/3$ (see [31] for more details). Additional attempts to use LBM in stability analysis are the works of Chang *et al.* [14] and Anupindi *et al.* [4], both of which monitor the time history of a given fluid variable during the simulation, from which it is determined whether the flow is unstable; none of these works employs a linearization of the numerical scheme in order to arrive at conclusions on flow stability. Closely related to the present work are those of Vergnault *et al.* [50] and Vergnault and Sagaut [51], who considered the SRT model and discussed the linearization of the evolution equation through the linearization of the direct and adjoint collision operators. Moreover, the former work proposed a nonlinear version of the disturbances in the physical space and it is worth exploring whether this formulation is equivalent with the linearized version of the Navier-Stokes equations around a given base flow.

The present work follows a time-stepping approach for global linear instability and presents, for the first time, two alternative linearizations of the local probability distribution function, one based on the classical function [43] which converges to the incompressible Navier-Stokes equations in the limit of vanishing Mach number, and another based on the function introduced by Hou et al. [30] that corresponds to the artificial compressibility equations proposed by Chorin [1], as well as the identification of all terms appearing in the linearized Navier-Stokes equations with those resulting from the different LBM linearizations under consideration of either of the SRT and MRT models. The residual algorithm [48] is employed to extract instability analysis results in two and three inhomogeneous spatial directions, while the Arnoldi algorithm has also been implemented and used to recover the eigenspectrum of the square and cubic lid-driven cavity flows, in order to compare with literature and arrive at conclusions regarding the suitability of a given LBM linearization model to perform global linear instability analysis.

The theoretical background is discussed in Section 2, where the derivation of the incompressible Navier-Stokes equations in a LBM context is shown in 2.1. Basics of global linear instability analysis are discussed in Section 2.2. Earlier formulations related with the global eigenvalue problem are presented in Section 2.3 followed in 2.4 by the presently proposed models. Two approaches to extract instability results from the DNS are discussed next, namely the residual algorithm in 2.5 and the Arnoldi algorithm. In Section 3 results obtained with the different linearized models applied to the square and cubic lid-driven cavity flow are discussed. Conclusions are presented in Section 4.

2 Theory

2.1 Navier-Stokes derivation

The derivation of the Navier-Stokes equations from those of the LBM is recalled in this section (see [16] for more details), since it will be useful in the subsequent derivation of the linearized Navier-Stokes equations (LNSE) in a LBM context. Throughout this section variables are defined in lattice units, while physical units are considered in Section 3. The relationship between both alternatives is described at the beginning of Section 3. The Chapman-Enskog multiscaling expansion assumes the existence of two time scales; convective (t_1) and viscous (t_2), such that $t_1 \ll t_2$ for any high-Reynolds number flow. The time derivative is thus split into two parts, corresponding to variations over t_1 and t_2,

$$\frac{\partial}{\partial t} = \epsilon \frac{\partial}{\partial t_1} + \epsilon^2 \frac{\partial}{\partial t_2}$$

where ϵ is the Knundsen number defined as the ratio between the lattice mean free path and the characteristic length scale of the problem. On the other hand, spatial derivatives are assumed that scale with ϵ,

$$\frac{\partial}{\partial x} = \epsilon \frac{\partial}{\partial x_1} .$$

For small ϵ, collisions dominate and the fluid remains close to the local equilibrium condition. Therefore, the following series exists and converges,

$$f_\alpha = f_\alpha^{(0)} + \epsilon f_\alpha^{(1)} + \epsilon^2 f_\alpha^{(1)} + \dots \tag{2}$$

Applying the above expressions to the evolution equation, the latter can be split into a set of equations valid at different orders of ϵ,

$$\begin{aligned} &O(\epsilon^0) : f_\alpha^{(0)} = f_\alpha^{eq} \,, \\ &O(\epsilon^1) : \left(\partial_{t_1} + \mathbf{e}_\alpha \cdot \nabla_1\right) f_\alpha^{(0)} + \frac{1}{\tau} f_\alpha^{(1)} = 0 \,, \\ &O(\epsilon^2) : \partial_{t_2} f_\alpha^{(0)} + \left(1 - \frac{1}{2\tau}\right)\left(\partial_{t_1} + \mathbf{e}_\alpha \cdot \nabla_1\right) f_\alpha^{(1)} + \frac{1}{\tau} f_\alpha^{(2)} \,. \end{aligned} \tag{3}$$

The first identity identifies the local equilibrium PDF with the first term of the series defined in (2). Introducing the expression at $O(\epsilon^0)$ into the first two statistical moments of the PDF, which by definition are equal to the density (ρ) and velocity ($\mathbf{u}$),

$$\rho = \sum_\alpha f_\alpha = \sum_\alpha f_\alpha^{eq} \,, \quad \rho\mathbf{u} = \sum_\alpha \mathbf{e}_\alpha f_\alpha = \sum_\alpha \mathbf{e}_\alpha f_\alpha^{eq} \,, \tag{4}$$

respectively, leads to the following constraints for the high terms of expansion (2),

$$\begin{aligned} &\sum_\alpha f_\alpha^{(0)} = \rho \,, \quad \sum_\alpha f_\alpha^{(i)} = 0 \,, \forall i > 0 \,. \\ &\sum_\alpha \mathbf{e}_\alpha f_\alpha^{(0)} = \rho\mathbf{u} \,, \quad \sum_\alpha \mathbf{e}_\alpha f_\alpha^{(i)} = 0 \,, \forall i > 0 \,. \end{aligned} \tag{5}$$

These relations restrict the form of $f_\alpha^{(0)}$, but not fully; additional relations are needed in order to define unequivocally this function. These are given by imposing the connection between the LB formulation and the Navier-Stokes equations. Defining $\mathit{\Pi}^{(n)}$ as,

$$\mathit{\Pi}_{i,j}^{(n)} = \sum_\alpha \mathbf{e}_\alpha^i \mathbf{e}_\alpha^j f_\alpha^{(n)} \,,$$

where $\mathbf{e}_\alpha^i$ is the i-component of vector $\mathbf{e}_\alpha$ the Euler equations are obtained by computing the sum of all velocity directions (α) of zeroth- and first-order moments of the relation obtained at order $O(\epsilon)$,

$$\frac{\partial \rho}{\partial t_1} + \nabla_1 \left(\rho\mathbf{u}\right) = 0 \,, \quad \frac{\partial \rho\mathbf{u}}{\partial t_1} + \nabla_1 \mathit{\Pi}^0 = 0 \,,$$

while the sum of all velocity directions of zeroth- and first-order moments of the relation obtained at $O(\epsilon^2)$ gives,

$$\frac{\partial \rho}{\partial t_2} = 0 \,, \quad \frac{\partial \rho\mathbf{u}}{\partial t_2} + \left(1 - \frac{1}{2\tau}\right) \nabla_1 \mathit{\Pi}^{(1)} = 0 \,.$$

The Navier-Stokes equations can be recovered by multiplying the first equation by ϵ, the second by ϵ^2 and adding these together, only when

$$\mathit{\Pi}_{i,j}^{(0)} = \sum_\alpha \mathbf{e}_\alpha^i \mathbf{e}_\alpha^j f_\alpha^{(0)} = \rho c_s^2 \delta_{i,j} + \rho u_i u_j \,, \tag{6}$$

$$\mathit{\Pi}_{i,j}^{(1)} = \sum_\alpha \mathbf{e}_\alpha^i \mathbf{e}_\alpha^j f_\alpha^{(1)} = -\tau \rho c_s^2 \left(\nabla_i(u_j) + \nabla_j(u_i)\right) \,, \tag{7}$$

where $c_s = c/\sqrt{3}$ is the characteristic sound speed (in lattice units) and $c = \Delta x/\Delta t$ that is, particles travel a distance Δx in a time Δt. Therefore, $\mathit{\Pi}^{(n)}$ can be identified with the flux-momentum tensor. Summing the different terms together leads to the Navier-Stokes equations,

$$\frac{\partial \rho}{\partial t} + \nabla (\rho \mathbf{u}) = 0 \,, \quad \frac{\partial \rho \mathbf{u}}{\partial t} + \nabla \Pi^{(0)} + \left(1 - \frac{1}{\tau}\right) \nabla \Pi^{(1)} = 0 \,. \tag{8}$$

Due to the dependence of f^1 on f^0 by the second equation of (3), these expressions plus the related to f^{eq} given in (4) define f^{eq}. Before continuing with the derivation, the discrete velocities $\mathbf{e}_\alpha$ must be defined.

The classical 9-velocity scheme (D2Q9) for two-dimensional problems and 19-velocity scheme (D3Q19) for three-dimensional problems, both represented in Figure 1, are considered in the discretization of the velocity directions performed in this work. For this configurations the velocity vectors ($\mathbf{e}_\alpha$) and weights (ω_α) for the D2Q9 model are given by,

$$(\mathbf{e}_\alpha, \omega_\alpha) = \begin{cases} ((0,0), & 4/9) & \alpha = 0 \\ (c(cos(\pi/4(\alpha-1)), sin(\pi/4(\alpha-1))), & 1/9) & \alpha = 1,2,3,4 \\ (c\sqrt{2}(cos(\pi/4(\alpha-1)), sin(\pi/4(\alpha-1))), & 1/36) & \alpha = 5,6,7,8 \end{cases}$$

and for the three-dimensional 19-velocity square lattice (D3Q19) are given by,

$$(\mathbf{e}_\alpha, \omega_\alpha) = \begin{cases} ((0,0,0), & 1/3) & \alpha = 0 \\ (c((\pm 1,0,0),(0,\pm 1,0),(0,0,\pm 1)), & 1/18) & \alpha = 1,2,\ldots 6 \\ (c((\pm 1,\pm 1,0),(\pm 1,0,\pm 1),(0,\pm 1,\pm 1)), & 1/36) & \alpha = 7,8,\ldots 18 \end{cases}$$

With these vectors, in the limit of small Mach numbers, the second-order approximation of f_α^{eq} is given by,

$$f_\alpha^{eq}(\rho, \mathbf{u}) = \omega_\alpha \rho \left(1 + \frac{\mathbf{e}_\alpha \cdot \mathbf{u}}{c_s^2} + \frac{(\mathbf{e}_\alpha \cdot \mathbf{u})^2}{2c_s^4} - \frac{\mathbf{u}^2}{2c_s^2}\right) . \tag{9}$$

where ω_α are the weights for the considered lattice molecule. The weights are associated with the set of discrete velocities and are used in order to take into account the different lengths of these vectors. In this formulation the pressure is given by the state equation of the ideal gas, $p = c_s^2 \rho$, where the adiabatic constant γ is equal to one. Finally, the relation between τ and μ is given by comparing (8) with the Navier-Stokes equations in the limit of small Mach number, $\nu = (2\tau - 1)/6\left(\Delta x^2/\Delta t\right)$. The last expression imposes that $\tau > 1/2$. Equation (9) defines the model hereinafter referred to as standard model.

Following the above choices, macroscopic quantities, such as density (ρ), velocity ($\mathbf{u}$) and stress tensor ($\mathbf{\Pi}$), are recovered as statistical moments of the particle distribution function. This is straightforward in the case of the first three relations (ρ, $\rho\mathbf{u}$ and $\Pi^{(0)}$), and approximated in $\Pi^{(1)}$. In the last case the $O(\epsilon)$ equation of (3) is introduced into the definition of $\Pi^{(1)}$ leading to

$$\Pi_{i,j}^{(1)} = -\tau \partial_{t_1} \left(\sum_\alpha \mathbf{e}_\alpha^i \mathbf{e}_\alpha^j f_\alpha^{eq}\right) - \tau \sum_\alpha \left(\nabla_{1,k} \cdot \mathbf{e}_\alpha^k\right) \mathbf{e}_\alpha^i \mathbf{e}_\alpha^j f_\alpha^{eq} \,.$$

Summing in α and using the following identity, $\sum_\alpha \mathbf{e}_\alpha^i \mathbf{e}_\alpha^j \mathbf{e}_\alpha^k f_\alpha^{eq} = \rho c_s^2 \left(u_i \delta_{j,k} + u_j \delta_{i,k} + u_k \delta_{i,j}\right)$, then,

$$\begin{aligned} \Pi_{i,j}^{(1)} = -\tau \left(c_s^2 \rho \left[\partial_{t_1} \rho + \nabla_{1,k} u_k\right] \delta_{i,j} + \rho c_s^2 \left[\nabla_{1,j} u_i + \nabla_{1,i} u_j\right]\right) \\ + \left[\partial_{t_1} \left(\rho u_i u_j\right) + \rho c_s^2 \left(u_j \nabla_{1,i} \rho + u_i \nabla_{1,j} \rho\right)\right] \,. \end{aligned}$$

The first term in the right hand side is the conservation of mass, therefore it must be equal to zero. The third term is $O(Ma^3)$ (see [30]), then equation (7) is correct up to $O(Ma^2)$.

On the other hand, this is a compressible formulation that in the low Mach number limit could be used in order to simulate weakly compressible flows, but only when precautions are taken [40]. This is a second order scheme in space and time [25,44], if compressibility effects (that scale with Ma^2) are negligible. Moreover, in the LBM the transport coefficients depend on the time step and lattice spacing, i.e., there is a numerical viscosity than is small as the number of cells increases.

In order to avoid numerical issues with the artificial compressibility introduced in the classical LBM, He and Lou [24] considered pressure and density as independent variables. These authors remove the terms of $O(Ma^2)$ responsible for density fluctuation existent in the previous models and proposed the following local equilibrium PDF which is derived using the same procedure described previously,

$$f_\alpha^{eq}(\rho, \mathbf{u}) = \omega_\alpha \rho + \omega_\alpha \rho_0 \left(\frac{\mathbf{e}_\alpha \cdot \mathbf{u}}{c_s^2} + \frac{(\mathbf{e}_\alpha \cdot \mathbf{u})^2}{2c_s^4} - \frac{\mathbf{u}^2}{2c_s^2} \right) . \tag{10}$$

ρ is the macroscopic density which fluctuates around the constant ρ_0. With this definition

$$\rho = \sum_\alpha f_\alpha = \sum_\alpha f_\alpha^{eq} , \quad \rho_0 \mathbf{u} = \sum_\alpha \mathbf{e}_\alpha f_\alpha = \sum_\alpha \mathbf{e}_\alpha f_\alpha^{eq} , \tag{11}$$

results and the macroscopic equations become

$$\frac{1}{c_s^2} \frac{\partial P}{\partial t} + \nabla \cdot \mathbf{u} = 0 , \quad \frac{\partial \mathbf{u}}{\partial t} + \mathbf{u} \cdot \nabla \mathbf{u} = -\nabla p + \nu \nabla^2 \mathbf{u} , \tag{12}$$

where $P = p/\rho_0$, ρ_0 is the density and $p = c_s^2 \rho$. This system of equations is the artificial compressibility model proposed by [1]. Equation (10) defines the model hereinafter referred to as the He–Lou model.

As discussed in the introduction, the SRT model has been widely used, however, due to its insufficient numerical stability for direct numerical simulations, the MRT approach was proposed [18,19] to increase the accuracy and stability presented by the LBGK scheme. The additional relaxation times could be adjusted in order to remove the numerical modes that arise in the numerical model on the grid scale.

A multiple set of relaxation times could be used instead of a single relaxation time. In the MRT model the right-hand side of Equation (1) is replaced by a collision operator, $\Omega(f)$ which takes place in each cell individually. In the SRT model this operator is equal to $-1/\tau I \left(\mathbf{f} - \mathbf{f}^{eq}\right)$, where I is the identity matrix and $\mathbf{f}$ (or $\mathbf{f}^{eq}$) are vectors of dimension equal to the number of directions considered in the lattice molecule. For instance, 9 and 19 when D2Q9 and D3Q19 models are considered for the two- and three-dimensional problems, respectively. In the case of the D2Q9 this vector is given by,

$$\mathbf{f} = (f_0, f_1, f_2, f_3, f_4, f_5, f_6, f_7, f_8) .$$

In the MRT model the collision operator is generalized by assuming that $\Omega(\mathbf{f}) = -S \left(\mathbf{f} - \mathbf{f}^{eq}\right)$, where S now is a matrix. This formulation increases the number of degrees of freedom in the modeling of the linearized collision operator and allows to use additional relaxation times in order to remove numerical instabilities arising from the truncation of the probability distribution function, see [34] for the two-dimensional case and [19] for the three-dimensional case. Instead of working in the probability distribution function space these authors proposed to work in the moment space in order to improve the performance of the method. Following the choice of components in the moment space considered by [34], the vector of moments is given by

$$\mathbf{m} = (\rho, e, \epsilon, j_x, j_y, q_x, q_y, p_{xx}, p_{xy}) ,$$

where ρ is the density, e is the energy, ϵ is the energy-square, j_x and j_y are the momentum in x- and y-direction, respectively, q_x and q_y are the heat flow in x- and y-direction and finally p_{xx} and p_{xy} are the diagonal and off-diagonal stress components (normal and tangential stress, respectively). The relation between these moments and the vector of PDF is given by a transform matrix M (see [34] when the D2Q9 model is considered). For this derivation the definition of the moments described earlier must be taken into account, as well as the relations between the physical variables and the PDFs. Matrix M transforms a vector of the velocity space into a vector of the moment space, $\mathbf{m} = M\mathbf{f}$, then the new expression of the linearized collision operator in the momentum space is

$$\Omega(\mathbf{f}) = -M^{-1} \hat{S} \left(\mathbf{m} - \mathbf{m}^{eq}\right) ,$$

where $\hat{S} = diag(s_0, \ldots, s_{q-1})$, is a diagonal matrix and s_i are the characteristics relaxation time parameters. An extensive discussion about the choice of parameters can be found in [19]. Therefore, using a MRT model, the lattice Boltzmann equation is given by,

$$\frac{\partial f_\alpha}{\partial t} + \mathbf{e}_\alpha \cdot \nabla f_\alpha = -M^{-1}\hat{S}\left(m_\alpha - m_\alpha^{eq}\right) . \tag{13}$$

Finally, one of the drawbacks of LBM is that in principle it is only defined for equidistant Cartesian grids. Even though grid refinement has been addressed by different authors in the lattice Boltzmann method community, this is not necessary in this work because the aim of this investigation is in studying the capability of this method to obtain modal instabilities by using a linearized version of the LBE around a steady base flow. For that reason, the square and cubic lid-driven cavity flows were chosen in order to be able to focus exclusively on stability issues, without the additional concern of domain mapping, metrics and local refinement. In the circular cylinder, equidistant Cartesian grids constitute a significant drawback in an LBM context, detailed discussion of which will be presented in future works.

2.2 Stability analysis

The equations of motion (8) or (12), can be written in a compact manner as,

$$\frac{\partial \mathbf{q}}{\partial t} = \mathbf{f}(\mathbf{q}) , \tag{14}$$

where $\mathbf{q} = (\rho, \mathbf{u})$ and $\mathbf{f}$ is the right hand side of the incompressible Navier-Stokes equations.

Linear stability theory studies the temporal evolution of small amplitude disturbances superimposed upon a base flow [49] where the flow is decomposed into a steady base flow $\overline{q} = (\overline{\rho}, \overline{\mathbf{u}})$ and a unsteady small perturbation $\mathbf{q}'$, then

$$\mathbf{q}(x,t) = \overline{\mathbf{q}}(x) + \mathbf{q}'(x,t) . \tag{15}$$

By introducing the decomposition of variables (15) into the governing equations (14) and neglecting the non-linear terms $O(\epsilon^2)$ or greater the linearized Navier-Stokes equations (LNSE) which determine the evolution of small perturbations are recovered. These equations can be written as initial-value-problem in the form,

$$\frac{\partial \mathbf{q}'}{\partial t} = \frac{\partial \mathbf{f}(\overline{q})}{\partial \mathbf{q}}\mathbf{q}' \equiv \mathbf{A}\mathbf{q}' , \tag{16}$$

where $\mathbf{A}$ is the Jacobian matrix of the right hand side of the Navier-Stokes equations and comprises the base flow and its spatial derivatives. In case of steady base flows, the separability between time and space coordinates permits a Fourier decomposition in time $\mathbf{q}' = \mathbf{q}'(\mathbf{x})e^{-i\omega t}$. Depending on the dimensionality of the base flow additional simplifications can be considered. In the present analyses, BiGlobal theory, which assumes the existence of two inhomogeneous and one homogeneous spatial direction is employed, as well as TriGlobal analysis, in which all three spatial directions are inhomogeneous (see [49] for more details). According to the BiGlobal Ansatz, solutions of the equation (16) are sought as eigenmodes

$$\mathbf{q}'(x,y,z,t) = \varepsilon\hat{\mathbf{q}}(x,y)\mathrm{e}^{\mathrm{i}(\beta z - \omega t)} + c.c. \tag{17}$$

where $\varepsilon \ll 1$, $\beta = 2\pi/L_z$ is the wavenumber in the spanwise spatial direction, z, $\hat{\mathbf{q}}$ are the eigenvectors and $\omega = \omega_r + \mathrm{i}\cdot\omega_i$, with ω_r representing a frequency and ω_i being the amplification/damping rate of the disturbance. In a TriGlobal analysis context, the decomposition

$$\mathbf{q}'(x,y,z,t) = \varepsilon\hat{\mathbf{q}}(x,y,z)\mathrm{e}^{-\mathrm{i}\omega t} + c.c. \tag{18}$$

replaces (17). In both cases, a large-scale non-Hermitian generalized eigenvalue problem (EVP) is obtained, by inserting equation (17) or (18) into equation (16), which reads

$$\mathbf{A}\hat{q} = \omega\mathbf{B}\hat{q} , \tag{19}$$

Two alternatives could be considered temporal or spatial evolution of the disturbances. The former (considered in the previous description) studies the evolution in time of a disturbance given as initial condition while spatial formulation studies the evolution in space of a disturbance given as inflow condition. The EVP obtained for spatial stability analysis is analogous to the temporal EVP but now β is complex and ω is real. Other difference is that the spatial stability problem have a non-linear dependence with β and the companion matrix defined by Bridges and Morris [12] must be used. In this work temporal BiGlobal and TriGlobal analysis will be considered.

There are two alternatives in order to solve the generalized eigenvalue problem; matrix-free and matrix-forming methods (see [49] for more details). Stability analysis is performed here by using time-stepping methods, which employ temporal integration of the perturbations using the linearized Navier-Stokes equations $\partial_t \mathbf{u}' = LNS_{\Delta t}\mathbf{u}'$ from 0 to t, which is equivalent to applying the exponential operator $exp\left(\int_0^t LNS_{\Delta t} dt\right)$ to the perturbation, $\mathbf{u}'$. Thus, the eigenvalue problem to be solved using the time-stepping method is defined by the exponential operator of the linearized version of the equations. The leading eigenvalue of the exponential operator to which the Arnoldi method converges is usually the most unstable or less stable eigenvalue of the linearized operator.

2.3 Linearization of the collision operator

Lallemand and Luo [34], Niu *et al.* [39] and Vergnault *et al.* [50] studied acoustics problems in weakly compressible flows by splitting the PDF in two parts, one corresponding to the steady base flow, $\overline{f}$, and another due to the unsteady part, f'. Assuming that the PDF of the base flow in equation (1) is steady, then

$$\mathbf{e}_\alpha \cdot \nabla \overline{f} = \frac{1}{\tau}\left(\overline{f}^{eq}_\alpha - \overline{f}_\alpha\right) .$$

Imposing $f = \overline{f} + f'$ in the evolution equation (1) and using the previous relation it is straightforward to obtain

$$\frac{\partial f'_\alpha}{\partial t} + \mathbf{e}_\alpha \cdot \nabla f'_\alpha = -\frac{1}{\tau}\left(f'_\alpha - f^{eq}_\alpha\right) - \frac{1}{\tau}\overline{f}^{eq}_\alpha , \tag{20}$$

where $\overline{f}^{eq}_i = f^{eq}_i(\overline{\rho}, \overline{\mathbf{u}})$. The previous equation could be used directly as the evolution equation for f'. However, as shown by Vergnault *et al.* [50] the macroscopic equations recovered from the evolution equation (20) result in a non-linear Navier-Stokes equations for the perturbation.

Another possibility can be obtained from the Taylor expansion of f^{eq}_α around $\overline{f}^{eq}_\alpha$, taking into account (17) or (18)

$$f^{eq}_\alpha = \overline{f}^{eq}_\alpha + \frac{\partial f^{eq}_\alpha}{\partial f_\beta}\Big|_{\overline{f}^{eq}_\alpha} f'_\beta, ...$$

in which $|f'| < |\overline{f}|$ is assumed. Substituting this relation in equation (20) yields to

$$\frac{\partial f'_\alpha}{\partial t} + \mathbf{e}_\alpha \cdot \nabla f'_\alpha = \frac{1}{\tau}\frac{\partial f^{eq}_\alpha}{\partial f_\beta}\Big|_{\overline{f}^{eq}_\alpha} f'_\beta - \frac{1}{\tau} f'_\alpha . \tag{21}$$

The expression for the resulting Jacobian has been calculated [34,39,51]),

$$\frac{\partial f^{eq}_\alpha}{\partial f_\beta} = \omega_\alpha \left(1 + \frac{\mathbf{e}_\alpha \cdot \mathbf{e}_\beta}{c_s^2} + \frac{1}{2c_s^4}\mathcal{H}^{(2)}_\alpha : (\mathbf{e}_\beta \mathbf{u} + \mathbf{u}\mathbf{e}_\beta - \mathbf{u}\mathbf{u})\right) ,$$

where $\mathcal{H}^{(2)}_{\alpha;i,j} = \mathbf{e}_{\alpha,i}\mathbf{e}_{\alpha,j} - c_s^2\delta_{ij}$ is the second Hermite polynomial. Although the above formulations appear in principle to be equivalent, in what follows they are treated as two different models in conjunction with the Arnoldi algorithm; Model I, given by equation (20) and Model II, given by equation (21).

2.4 Linearization of the local equilibrium PDF

The derivation of the Navier-Stokes equations shown in Section 2.1 is followed here in order to derive the linearized Navier-Stokes equations (LNSE) in the limit of low Mach number. In this case, instead of equations (4), (6) and (7) the following relations are imposed

$$\sum_\alpha f'_\alpha = \sum_\alpha f'^{eq}_\alpha = \rho' \,, \quad \sum_\alpha \mathbf{e}_\alpha f'_\alpha = \sum_\alpha \mathbf{e}_\alpha f'^{eq}_\alpha = \overline{\rho} u' + \rho' \overline{\mathbf{u}} \,, \tag{22}$$

$$\Pi'^0_{i,j} = \sum_\alpha \mathbf{e}^i_\alpha \mathbf{e}^j_\alpha f'^{(0)}_\alpha = \rho' c_s^2 \delta_{i,j} + \rho' \, \overline{u}_i \, \overline{u}_j + \overline{\rho} \, u'_i \, \overline{u}_j + \overline{\rho} \, \overline{u}_i \, u'_j \,, \tag{23}$$

$$\Pi'^1_{i,j} = \sum_\alpha \mathbf{e}^i_\alpha \mathbf{e}^j_\alpha f'^{(1)}_\alpha = -\tau \overline{\rho} c_s^2 \left(\nabla_i u'_j + \nabla_j u'_i \right) - \tau \rho' c_s^2 \left(\nabla_i \overline{u}_j + \nabla_j \overline{u}_i \right) \,, \tag{24}$$

leading to redefinition of the local equilibrium PDF. Furthermore, the resulting equations in the physical space are

$$\frac{\partial \rho'}{\partial t} + \nabla \left(\rho' \overline{\mathbf{u}} + \overline{\rho} \mathbf{u}' \right) = 0 \,, \quad \frac{\partial \rho' \overline{\mathbf{u}} + \overline{\rho} \mathbf{u}'}{\partial t} + \nabla \Pi'^{(0)} + \left(1 - \frac{1}{\tau} \right) \nabla \Pi'^{(1)} \,. \tag{25}$$

where second order terms in perturbation have been neglected, and,

$$\Pi^{(n)} = \sum_\alpha \mathbf{e}_\alpha \mathbf{e}_\alpha \overline{f}^{(n)}_\alpha + \sum_\alpha \mathbf{e}_\alpha \mathbf{e}_\alpha f'^{(n)}_\alpha + O(\varepsilon^2) \,.$$

Note that $p' = c_s^2 \rho'$. Then, the integration of the evolution equation,

$$\frac{\partial f'_\alpha}{\partial t} + \mathbf{e}_\alpha \cdot \nabla f'_\alpha = -\frac{1}{\tau} \left(f'_\alpha - f'^{eq}_\alpha \right) \,, \tag{26}$$

is equivalent to the integration of equations (25). In order to close the system, the local equilibrium PDF must be found. Starting from the more general equation,

$$\begin{aligned} f'^{eq}_\alpha = \rho' w_\alpha \Big(c_1 + c_2 \, \mathbf{e}_\alpha \cdot \overline{\mathbf{u}} + c_3 \left(\mathbf{e}_\alpha \cdot \overline{\mathbf{u}} \right)^2 + c_4 \, \overline{\mathbf{u}} \cdot \overline{\mathbf{u}} \Big) + \\ \overline{\rho} w_\alpha \left(c_5 + c_6 \, \mathbf{e}_\alpha \cdot \mathbf{u}' + c_7 \left(\mathbf{e}_\alpha \cdot \mathbf{u}' \right) \left(\mathbf{e}_\alpha \cdot \overline{\mathbf{u}} \right) + c_8 \, \mathbf{u}' \cdot \overline{\mathbf{u}} \right) \,, \end{aligned}$$

the coefficients that allow to meet (22), (23) and (24) are identified, and the following relationship holds

$$f'^{eq}_\alpha = \frac{\rho'}{\overline{\rho}} \overline{f}^{eq}_\alpha + \overline{\rho} w_\alpha \left(\frac{\mathbf{e}_\alpha \cdot \mathbf{u}'}{c_s^2} + \frac{\left(\mathbf{e}_\alpha \cdot \mathbf{u}' \right) \left(\mathbf{e}_\alpha \cdot \overline{\mathbf{u}} \right)}{c_s^4} - \frac{\mathbf{u}' \cdot \overline{\mathbf{u}}}{c_s^2} \right) \,, \tag{27}$$

where the following equations have been used

$$\sum_\alpha \mathbf{e}^i_\alpha \mathbf{e}^j_\alpha \mathbf{e}^k_\alpha f'^{eq}_\alpha = \overline{\rho} c_s^2 \left(u'_i \delta_{j,k} + u'_j \delta_{i,k} + u'_k \delta_{i,j} \right) + \rho' c_s^2 \left(\overline{u}_i \delta_{j,k} + \overline{u}_j \delta_{i,k} + \overline{u}_k \delta_{i,j} \right) \,. \tag{28}$$

As happens in the general case, terms $O(Ma^3)$ are neglected in the evaluation of $\Pi'^{(1)}_{i,j}$ and ν has the same relation with τ. In the same manner the following identity is derived from the model (10),

$$f'^{eq}_\alpha = \rho' w_\alpha + \rho_0 w_\alpha \left(\frac{\mathbf{e}_\alpha \cdot \mathbf{u}'}{c_s^2} + \frac{\left(\mathbf{e}_\alpha \cdot \mathbf{u}' \right) \left(\mathbf{e}_\alpha \cdot \overline{\mathbf{u}} \right)}{c_s^4} - \frac{\mathbf{u}' \cdot \overline{\mathbf{u}}}{c_s^2} \right) \,. \tag{29}$$

These two models are defined in this work as Model III and Model IV, respectively. Imposing $f_\alpha = \overline{f}_\alpha + f'_\alpha$ in Equation (13), where $\overline{f}$ is the probability distribution function given by the base flow and f' the corresponding for the perturbation, and due to the linearity of the equation, the contribution given by the base flow factorized and the expression for the perturbation is,

$$\frac{\partial f'_\alpha}{\partial t} + \mathbf{e}_\alpha \cdot \nabla f'_\alpha = -M^{-1} \hat{S} \left(m'_\alpha - m'^{eq}_\alpha \right) \,, \tag{30}$$

where $\mathbf{m}' = M \mathbf{f}'$. Note that the same relaxation time parameters considered in the non-linear LBE are valid in the linear LBE.

2.5 Residual algorithm

Least-damped eigenmode properties such as the damping rate, frequency and amplitude function can be recovered by analyzing the numerical residual of direct numerical simulations when the flow is close to the steady solution, $\overline{q}$ (see [48]). The linearized equations are recovered by replacing this decomposition in the Navier-Stokes equations and neglecting terms greater than $O(\varepsilon^2)$. Taking $\beta = 0$ in the Ansatz (17),

$$\mathbf{q}'(x,y,t) = \hat{\mathbf{q}}(x,y)e^{-i\omega t} = (\hat{q}_r(x,y)cos\,(\omega_r t) - \hat{q}_i(x,y)sin\,(\omega_r t))\,e^{\omega_i t}\,. \tag{31}$$

The value of ω_i can be recovered without additional manipulations when $\omega_r = 0$ by using $\omega_i \approx d|q(x,y,t) - \overline{q}(x,y)|/dt$. In the general case when $\omega_r \neq 0$, the process is a little more involved, see [48] for more details. The perturbations amplitude functions can be obtained by the combination of the solution at two different times, t_1 and t_2:

$$\hat{q}_r = \frac{1}{\varepsilon}\frac{s_1\Delta q_2 - s_2\Delta q_1}{c_2 s_1 - c_1 s_2}\,, \quad \hat{q}_i = \frac{1}{\varepsilon}\frac{c_1\Delta q_2 - c_2\Delta q_1}{c_2 s_1 - c_1 s_2} \tag{32}$$

where $\Delta q_i = q_i - \overline{q}$, $c_i = e^{\omega_i t_i}cos(\omega_r t_i)$ and $s_i = e^{\omega_i t_i}sin(\omega_r t_i)$.

3 Results

3.1 Base flow

Throughout this section variables are defined in physical units. The relationships that allow to pass variables from lattice units to physical units are described below. The Reynolds number is defined as $Re = U_0 L_0/\nu_0$ where U_0, length L_0 and ν_0 are the characteristic physical velocity, length and kinematic viscosity, respectively. In physical units, $\Delta x_{phy} = L_0/N$, where N is the number of lattice molecules in x direction and $\Delta t_{phy} = (\Delta x^2_{phy}/\nu_{phy})(2\tau - 1)/6$. In lattice units, $u = (\Delta t_{phy}/\Delta x_{phy})u_{phy}$ and $\nu = (\Delta t_{phy}/\Delta x^2_{phy})\nu_{phy} = (2\tau - 1)/6$. Since Reynolds number must be the same, and this is equal to UL/ν in lattice units, then $L = N$, which implies that $\Delta x = 1$ with this choice.

The LBM has been extensively employed to simulate flow in the square and the cubic lid-driven cavity, both of which are classic benchmark geometries in which a variety of phenomena arise: flow instabilities, corner eddies and transition to turbulence. Hou *et al.* [30] used the LBM in the range $10 \leq Re \leq 10^4$, while Hou [29] simulated the cubic cavity flow at $Re = 3200$ using a 15-velocity model. Direct numerical simulations show that the two-dimensional flow is unstable at a critical Reynolds number $Re_{\mathrm{cr,2d}} \approx 8026$ [9] while the three-dimensional flow is unstable via a symmetry-breaking subcritical Hopf bifurcation at $Re_{\mathrm{cr,3d}} \approx 1914$ [21].

The test cases considered in this work are the sub-critical 2D flow at $Re = 1000$ and 3D flow at $Re = 200$. In both cases the singular cavity version, $u_{top} = 1$ has been used. The steady base flow solution is obtained using the standard model, equation (9), as well as the He and Luo model [24], equation (10), in conjunction with SRT and MRT. In MRT the relaxation times are those proposed by Lallemand and Luo [34] while in the SRT model $\tau = 2/3$ was chosen in all the simulations.

Following the classical procedure, temporal integration is performed in two steps, starting with the collision step ($\tilde{f}_\alpha(x_i,t) = f_\alpha(x_i,t) - 1/\tau(f_\alpha(x_i,t) - f^{eq}_\alpha(x_i,t))$ and followed by the streaming (convective) step ($f_\alpha(x_i + e_\alpha\delta t, t + \delta t) = \tilde{f}(x_i,t)$). While the collision process is local and conservative (conserves mass and momentum), the streaming step is non-local and may lead to propagation of particles between collisions. The bounce-back boundary condition is used to simulate no-slip at stationary walls and its generalization for moving walls, proposed by Bouzidi et al. [11], is used at the moving boundary.

The two-dimensional lid-driven cavity flow is defined in the unit square $(x,y) \in [0,1]^2$ and was resolved using grids comprising 200^2, 300^2 and 400^2 discretization nodes in order to ensure convergence. The simulations showed that a mesh size of 200^2 is sufficient for convergence of the base flow and its first derivatives. Regarding the CFL number, consistency between the LBM formulation and the

Navier-Stokes equations imposes that $\Delta t = CFL\left(\Delta x^2/\nu\right)$ where the term between brackets could be interpreted as the viscous time step and CFL is the Courant−Friedrichs−Lewy number which is equal to $(\tau - 1/2)/3$ in the case of the molecule D2Q9 considered in the two-dimensional work.

The magnitudes and locations of the center of the primary vortex are shown in Table 1 where good agreement with the results of Ghia *et al.* [22] can be seen. Analogous results were obtained using equation (10) as local equilibrium PDF. The $\bar{u}$ and $\bar{v}$ velocity profiles at the $y-$ and $x-$axis center-lines, obtained using the standard LBM model (9) and 200 molecules in each spatial direction are compared with the tabulated results of [22] in Figure 2. In the same figure the comparison of results obtained using the SRT and MRT models is shown, also with satisfactory results.

The three-dimensional lid-driven cavity flow defined in the cube $(x, y, z) \in [0, 1]^3$ is discretized by the D3Q19 molecule and is subjected to the velocity boundary conditions discussed by Hecht and Harting [26], a generalization of those proposed by Zou and He [56]. The bounce-back boundary condition is used at the stationary walls. Validation data for this problem is provided by Albensoeder and Kuhlmann [2] and Shapeev *et al.* [45]. Figure 3 shows the streamline patterns on the three center planes of the cavity, obtained with the three-dimensional LBM and a resolution of 150^3; again good qualitative and quantitative (not shown here) agreement has been obtained with literature results.

Finally, the simulations performed with He-Lou model show that the mean velocity divergence in the square lid-driven cavity at Reynolds 1000 is 3×10^{-3} and 1×10^{-3} at resolutions 300^2 and 400^2, respectively. As has been discussed previously, the lattice Boltzmann model converge to the macroscopic Navier-Stokes equations with a truncation error of second order in Ma number, therefore these values can be used in order to evaluate the compressibility effect. The mean velocity divergence obtained at resolutions 300^2 and 400^2 is consistent with the values presented in Table 6 by [55] for the He-Lou model, which implies that the deviation is $O(Ma^2)$, which is consistent with the overall error committed by the LBM.

3.2 Stability Analysis

Several simulations have been performed in order to identify the leading mode of the base flows calculated in the previous section. In order to monitor the convergence of the numerical solution, the value of the $\bar{u}$ velocity component at the center of the cavity was used. As discussed in section 2.5, the residual (the logarithm of the relative error between the converged solution and the solution at a given time), delivers the damping rate of the leading steady mode. Figure 4 shows the time-evolution of the residual, as obtained in LBM simulations using standard and He and Luo [24] local equilibrium PDF function in conjunction with either of the SRT and MRT models. Two important conclusions may be drawn. First, focusing on the region at times between 100 and 200 it is seen that the damping rates obtained using SRT and MRT are the same in the first two significant figures and very close to the result obtained using the time-stepping stability module of Semtex (see [8,7] for more details). As can be seen in Table 2 the relative error is less that 1% in all cases. Second, all models predict spurious numerical modes at long integration times.

Figure 5 shows a comparison between the $\hat{u}$ and $\hat{v}$ amplitude functions of the leading mode in the square lid-driven cavity at $Re = 1000$, obtained by the spectral code and either of the LBM codes with the SRT or the MRT models, the latter using (32). As can be seen, good qualitative agreement exists between all results although the MRT model recovers the eigenmode structure more accurately than the SRT model; on the other hand, the MRT exhibits numerical instabilities in the streamlines that are absent in the SRT result.

Turning to solution of the eigenvalue problem in a time-stepping framework, the reverse communication interface for Arnoldi iteration provided in ARPACK [36] was used with the linear evolution operators defined as Model I, equation (20), and Model II, equation (21), as well as using the local equilibrium PDF proposed in this work, Model III and Model IV, respectively defined by equations (27) and (29). The boundary conditions imposed on the first two models were proposed by Vergnault et al. [50]. In this case the local equilibrium PDF is added to f', then boundary conditions are applied and finally the contribution of the local equilibrium PDF at the boundaries is removed. In the

presently proposed models the bounce-back ([53,35]), which mimics a no-slip boundary condition is applied directly to f' due to the linearity of the equations.

Regarding the cubic lid-driven cavity flow, a preliminary study employing the residuals algorithm concerns the ability of the linear Models III and IV to recover the least damped modes, starting from a steady base flow at $Re = 100$ with a small random perturbation added. The latter field used in these simulations comprised boundary condition perturbations for velocity and pressure, whose maximum and minimum values for density and velocity are $7 \times 10^{-8} - 2.3 \times 10^{-7}$ and $0 - 10^{-5}$, respectively. Figure 6 shows that while model IV recovers the damping rate of the leading mode, Model III also recovers the same at short times but, in addition, produces a spurious numerical mode with slow decay at long times. The damping rate of the leading mode in this configuration, given by the spectral code, is equal to $\omega_{\mathrm{i}} = -0.54131$. As the linear curve fits of Figure 6 show, Model IV predicts a value of $\omega_{\mathrm{i,IV}} = -0.530$ while Model III predicts a much less accurate damping rate of $\omega_{\mathrm{i,III}} = -0.511$ at short times and, in addition, a spurious mode with $\omega_{\mathrm{i}} = -0.053$ at long times.

Next, solution of the two-dimensional eigenvalue problem was performed using a Krylov subspace dimension of 40, Arnoldi tolerance equal to 10^{-5}, total integration time on each Arnoldi iteration equal to 10, and maximum number of iterations of 500. Neither of Models I or II converged, while Models III and IV did converge and delivered the results shown in figures 7, 8 and 9. It can be seen that the amplitude functions of the first mode are in qualitatively good agreement with the results obtained with the spectral code, see left column of Figure 5 (up for $\hat{u}$ and down for $\hat{v}$). Table 4 provides the numerical values of the damping rates obtained using the linearized formulations in conjunction with the Arnoldi algorithm. Table 3 shows the same study at $Re = 100$.

Finally, instability in the cubic lid-driven cavity was addressed with the same two approaches, application of the residual algorithm to the results of the direct numerical simulation as the latter approaches convergence, and solution of the three-dimensional global eigenvalue problem using the Arnoldi algorithm. Figure 10 shows the three-dimensional reconstruction of the leading mode obtained from the residuals algorithm at $Re = 1000$ and figures 11 and 12 show the reconstruction of the leading mode obtained from three-dimensional eigenvalue problem using the Arnoldi algorithm at $Re = 200$. Both reconstructions show good qualitative agreement with three-dimensional literature results. The damping rate result obtained from solution of the eigenvalue problem at $Re = 200$ is presented in Table 5 and is compared with the result shown by Gómez et al. [20] who used a time-stepping method and the OpenFOAM open source software to analyze instability in a variable aspect ratio three-dimensional lid-driven cavity; reasonable agreement can be seen here too.

The incompressible LBM considered in this work are a limit case of a compressible formulation, implying a weak formulation of the boundary condition. This often generates mass variation in the computational domain and non-physical results, which interferes with linear stability analysis. Bergamo et al. [6] studied this problem in the square lid-driven cavity for low Mach numbers noting both that compressibility has a stabilizing effect and modes related with the energy equation, not present in the incompressible limit, arise at low Mach numbers. This effect may be responsible for the observed discrepancies in the results between the linearized LBM and the spectral code obtained in this work, and should be considered in future research.

To demonstrate the capability of the linearized LBM to recover global linear instability analysis in open flows, the proposed methodology has been applied to two-dimensional flow around a circular cylinder with unit radius, as considered by [28]. The inlet velocity in the streamwise direction x is set equal to one by using the model proposed by [56], periodic, outflow and far-field boundary conditions have been considered in the top and bottom boundaries, while at the outflow boundary the condition suggested by [54] and modified by [32] is employed where zero pressure Dirichlet and zero velocity Neumman conditions are imposed. The cylinder is set into an initially uniform flow with velocity equal to one. The inner boundary is treated in an immersed boundary methodology and follows the interpolation-based model for curved geometries given by [11]. This model considered bounce-back and interpolation methods for treating curved boundaries as rigid walls with no-slip velocity. Finally, the computational domain considered in the simulations is $0 < x < 40$ and $0 < y < 20$, where the center of the cylinder located at the position $(10, 10)$.

Preliminary simulations were performed in order to demonstrate the validity of the boundary conditions considered in this problem. For example, a Strouhal number of the vortex shedding equal to 0.186 was obtained at Reynolds 150 and resolution $N_x \times N_y = 1200 \times 600$, a value that is within 0.05% of that shown in [52]; the length of the recirculation bubble at $y = 0$ is 2.23, which is within 1.4% from the spectral prediction of 2.27. Figure 13 shows the streamline patterns and the streamwise velocity component at $Re = 40$. The residual algorithm is then employed to the DNS results in order to obtain the damping rate of the leading mode and the result obtained using model IV (SRT) is shown in Figure 14. The relative discrepancy of our result and the value $\omega_{\mathrm{i}} = -0.02846$ obtained from the linearized version of the spectral code is about 12% at the parameters used.

4 Conclusions

A time-stepping solver based on linearization of the local equilibrium probability distribution function in the lattice Boltzmann method has been derived and applied for the first time to successfully perform global linear instability analysis. The well-studied square and cubic lid-driven cavity has been used to demonstrate the proposed methods. As with time-stepping solvers based on traditional numerical methods for spatial discretization of the linearized Navier-Stokes equations, the Jacobian is computed and the linearized equations of motion are time-advanced in order to construct Krylov subspaces from which the eigenvalue problem results are extracted. The novelty of the present work is in the computation of the Jacobian, which proceeds by first decomposing steady and unsteady parts of the probability distribution function (PDF), and subsequently linearizing the total PDF around that of the base flow. The single and multiple relaxation time models have been incorporated in this framework in an attempt to recover the well-known global eigenmodes of the benchmark configurations addressed. It is found that previously proposed models based on the linearization of the collision operator are not suitable to perform modal global instability analysis, while the presently proposed linearization of the local PDF permits recovering known results in both closed and open geometries. Further work is underway in order to obtain boundary conditions which increase the accuracy by which the LBM reproduces flow instability analysis results obtained by spectral methods.

References

1. Chorin A.J. A numerical method for solving incompressible viscous flow problems. *Journal of Computational Physics*, 2:12–26, 1967.
2. S. Albensoeder and H.C. Kuhlmann. Accurate three-dimensional lid-driven cavity flow. *Journal of Computational Physics*, 206(2):536–558, 2005.
3. F.J. Alexander, S. Chen, and J.D. Sterling. Lattice Boltzmann thermohydrodynamics. *Phys. Rev. E*, 47:R224952, 1993.
4. K. Anupindi, W. Lai, and S. Frankel. Characterization of oscillatory instability in lid driven cavity flows using lattice Boltzmann method. *Computers & Fluids*, 92:721, 2014.
5. R. Benzi, S. Succi, and M. Vergassola. The lattice Boltzmann equation: theory and applications. *Physics Reports*, 222(3):145197, 1992.
6. L.F. Bergamo, E.M. Gennaro, V. Theofilis, and M.A.F. Medeiros. Compressible modes in a square lid-driven cavity. *Aerospace Science and Technology*, 44:125–134, 2015.
7. H.M. Blackburn. Study of two-dimensional flow past an oscillating cylinder. *J. Fluid Mech.*, 385:255–286, 1999.
8. H.M. Blackburn. Three-dimensional instability and state selection in an oscillatory axisymmetric swirling flow. *Phys. Fluids*, 14(11):39833996, 2002.
9. V. B. L. Boppana and J. S. B. Gajjar. Global flow instability in a lid-driven cavity. *Int. J. Numer. Meth. Fluids*, 62(8):827–853, 2009.
10. M. Bouzidi, D. d'Humieres, P. Lallemand, and L-S Luo. Lattice Boltzmann equation on a two-dimensional rectangular grid. *Journal of Computational Physics*, 172:704–717, 2001.
11. M. Bouzidi, M. Firdaouss, and P. Lallemand. Momentum transfer of a Boltzmann-lattice fluid with boundaries. *Phys. Fluids*, 13:3452–, 2001.
12. T. Bridges and P. Morris. Differential eigenvalue problems in which the parameter appears nonlinearly. *J. Comput. Phys.*, (55):437–, 1984.
13. C. Canuto, M. Y. Hussaini, A. Quarteroni, and T. A. Zang. *Spectral Methods. Fundamentals in Single Domains.* Springer, 2006.
14. H.-W. Chang, P.-Y. Hong, L.-S., and C.-A. Lin. Simulations of flow instability in three dimensional deep cavities with multi relaxation time lattice Boltzmann method on graphic processing units. *Computers & Fluids*, 88:866871, 2013.
15. S. Chapman and T.G. Cowling. *The mathematical theory of non-uniform gases.* Cambridge Mathematical Library, 1991.
16. S. Chen and G.D. Doolen. Lattice Boltzmann method for fluid flows. *Annual Reviews of Fluid Mechanics*, 30:329364, 1998.
17. Y. Chen, H. Ohashi, and M. Akiyama. Thermal lattice bhatnagar-gross-krook model without nonlinear deviations in macrodynamic equations. *Phys. Rev. E*, 0:2776-83, 1994.
18. D. d'Humieres. Generalized lattice Boltzmann equations. in rarefied gas dynamics: theory and simulations. *Prog. Aeronaut. Astronaut. (ed. B. D. Shizgal & D. P.Weaver)*, 159:450458, 1992.
19. D. d'Humieres. Multiple-relaxation-time lattice Boltzmann models in three dimensions. *Phil. Trans. R. Soc. Lond A*, 360(1792), 2002.
20. Gómez F., R. Gómez, and V. Theofilis. On three-dimensional global linear instability analysis of flows with standard aerodynamics codes. *Aerospace Science and Technology*, 32:223234, 2014.
21. A.Y. Feldmana, Y.and Gelfgat. Oscillatory instability of a three-dimensional lid-driven flow in a cube. *Physics of Fluids*, 22:093602–, 2010.
22. U. Ghia, Ghia L., and C.T. Shin. High-re solutions for incompressible flow using the Navier-Stokes equations and a multigrid method. *Journal of Computational Physics*, 48:387–411, 1982.
23. Fasel H. Investigation of the stability of boundary layers by a finite-difference model of the Navier-Stokes equations. *Journal of Fluid Mechanics*, 78:335383, 1976.
24. X.Y. He and L.-S. Luo. Lattice Boltzmann model for the incompressible NavierStokes equation. *J. Stat. Phys.*, 88:927944, 1997.
25. X.Y. He and L.-S. Luo. Theory of the lattice Boltzmann method: from the Boltzmann equation to the lattice Boltzmann equation. *Physical Review E*, 56:68116817, 1997.
26. M. Hecht and J. Harting. Implementation of on-site velocity boundary conditions for d3q19 lattice Boltzmann. *Journal of Statistical Mechanics: theory and experiment*, page P01018, 2010.
27. F.J. Higuera and J. Jiménez. Boltzmann approach to lattice gas simulations. *Europhys. Lett.*, 9:663–668, 1989.
28. F.J. Higuera and S. Succi. Simulating the flow around a circular cylinder with a lattice Boltzmann. *Europhys. Lett.*, 9:345–349, 1989.
29. S. Hou. *Lattice Boltzmann method for incompressible viscous flow.* PhD thesis, Kansas State Univ., Manhattan, Kansas, 1995.
30. S. Hou, Q. Zou, S. Chen, G. Doolen, and A. Cogley. Simulation of cavity flow by the lattice Boltzmann method. *Journal of Computational Physics*, 118:329347, 1995.
31. D. James and C. Shiyi. Stability analysis of lattice Boltzmann methods. *Publication: eprint arXiv:comp-gas/9306001 Publication Date: 06/1993.*
32. M. Junk and Z. Yang. Asymptotic analysis of lattice boltzmann outflow treatments. *Commun. Comput. Phys.*, 9(5):1117–1127, 2011.
33. L. Kleiser and U. Schumann. Treatment of incompressibility and boundary conditions in 3D numerical spectral simulations of plane channel flows. In E. H. Hirschel (Vieweg and 1980) Sohn, Braunschweig, editors, *Proceedings of the Third GAMM Conference on Numerical Methods in Fluid Mechanics*, pages 165–173, 1980.

34. P. Lallemand and L.-S. Luo. Theory of the lattice Boltzmann method: Dispersion, dissipation, isotropy, galilean invariance, and stability. *Phys. Rev. E*, 61:6546–6562, 2000.
35. P. Lavalle, J.P. Boon, and A. Noullez. Boundaries in lattice gas flows. *Physica D*, 47:233–240, 1991.
36. R.B. Lehoucq, D.C. Sorensen, and C. Yang. *Arpack Users Guide: Solution of Large-Scale Eigenvalue Problems with Implicitly Restarted Arnoldi Methods*. SIAM Piladelphia, 1998.
37. G.R. McNamara, A.L. Garcia, and B.J. Alder. Stabilization of thermal lattice Boltzmann models. *J. Stat. Phys.*, 81:395408, 1995.
38. G.R. McNamara and G. Zanneti. Use of the Boltzmann equation to simulate lattice-gas automata. *Phys. Rev. Lett.*, 61:23322335, 1988.
39. X. D. Niu, C. Shu, Y.T. Chew, and T.G. Wang. Investigation of stability and hydrodynamics of different lattice Boltzmann models. *Journal of Statistical Physics*, 177(N 3/4), 2004.
40. R.R. Nourgaliev, T.N. Dinh, T.G. Theofanous, and D. Joseph. The lattice Boltzmann equation method: theoretical interpretation, numerics and implications. *International Journal of Multiphase Flow*, 29:117–169, 2003.
41. S. A. Orszag and L. C. Kells. Transition to turbulence in plane poiseuille flow and plane couette flow. *Journal of Fluid Mechanics*, 96:159205, 1980.
42. Y.H. Qian. Simulating thermohydrodynamics with lattice bgk models. *J. Sci. Comput.*, 8:231–242, 1993.
43. Y.H. Qian, D. d'Humieres, and P. Lallemand. Lattice bgk models for Navier-Stokes equation. *Europhys. Lett.*, 17:479–484, 1993.
44. X. Shan, X.-F. Yuan, and H. Chen. Kinetic theory representation of hydrodynamics: a way beyond the Navier-Stokes equation. *Journal of Fluid Mechanics*, 550:413–441, 2006.
45. V.P Shapeev and E.V. Vorozhtsov. Cas application to the construction of the collocations and least residuals methods for the solution of 3d Navier-Stokes equations. In *Computer Algebra in Scientific Computing: 15th International Workshop, CASC 2013*, Berlin, Germany, September 9-13, 2013.
46. J.D. Sterling and C. Shiyi. Stability analysis of lattice Boltzmann methods. *Journal of Computational Physics*, 123:196–206, 1996.
47. S. Succi. *The Lattice Boltzmann Equation for Fluid Dynamics and Beyond*. Clarendon Press, 2001.
48. V. Theofilis. On steady state flow solutions and their non-parallel global linear instability. In C. Dopazo et al., editor, *Advances in Turbulence VIII. Proceedings of the 8th European Turbulence Conference*, pages 35–38, Barcelona, Spain, 2000.
49. V. Theofilis. Global linear instability. *Annual Reviews of Fluid Mechanics*, 43:319–352, 2011.
50. E. Vergnault, O. Malaspinas, and P. Sagaut. A lattice Boltzmann method for nonlinear disturbances around an arbitrary base flow. *Journal of Computational Physics*, 231:80708082, 2012.
51. E. Vergnault and P. Sagaut. An adjoint-based lattice Boltzmann method for noise control problems. *Journal of Computational Physics*, 276:3961, 2014.
52. C.H.K. Williamson. Defining a universal and continuous StrouhalReynolds number relationship for the laminar vortex shedding of a circular cylinder. *Phys. Fluids*, 31:2742–, 1988.
53. S. Wolfram. Cellular automaton fluids. 1: Basic theory. *J. Stat. Phys.*, 45:471–526, 1986.
54. Z. Yang. Lattice boltzmann outflow treatments: Convective conditions and others. *Computers and Mathematics with Applications*, 65:160–171, 2013.
55. L. Zhang, Z. Zeng, H. Xie, Yo. Zhang, Y. Lu, A. Yoshikawa, H. Mizuseki, and Y. Kawazoe. A comparative study of lattice Boltzmann models for incompressible flow. *Computers and Mathematics with Applications*, 68:14461466, 2014.
56. Q. Zou and X. He. On pressure and velocity boundary conditions for the lattice Boltzmann bgk model. *Phys. Fluids.*, 9(6):15911598, 1997.

Table 1 Comparison of the primary vortex center location in the square lid-driven cavity obtained with the different LBM models and Ghia et al. [22] at $Re = 1000$.

	Model III (SRT)			Model III (MRT)		
$N_x \times N_y$	x	y	ω_z	x	y	ω_z
200×200	0.5322 ± 0.001	0.5677 ± 0.001	-2.05948	0.5322 ± 0.001	0.5675 ± 0.001	-2.06554
300×300	0.5317 ± 0.001	0.5653 ± 0.001	-2.05715	0.5314 ± 0.001	0.5655 ± 0.001	-2.06027
400×400	0.5313 ± 0.001	0.5664 ± 0.001	-2.05773	0.5312 ± 0.001	0.5654 ± 0.001	-2.05987
	Model IV (SRT)			Model IV (MRT)		
	x	y	ω_z	x	y	ω_z
200×200	0.5322 ± 0.001	0.5637 ± 0.001	-2.05908	0.5319 ± 0.001	0.5641 ± 0.001	-2.06374
300×300	0.5317 ± 0.001	0.5652 ± 0.001	-2.05615	0.5317 ± 0.001	0.5652 ± 0.001	-2.05915
400×400	0.5311 ± 0.001	0.5653 ± 0.001	-2.05690	0.5313 ± 0.001	0.5652 ± 0.001	-2.05912
				Ghia et al.		
				x	y	ω_z
256×256				0.5313	0.5625	-2.04968

Table 2 Damping rate of the leading mode of the square lid-driven cavity at $Re = 1000$ obtained using the residual algorithm [48]. Semtex uses 124^2 spectral collocation points. $a.b(c) = a.b \times 10^c$.

$N_x \times N_y$	Model III (SRT)	Model III (MRT)	Model IV (SRT)	Model IV (MRT)	Semtex
200×200	-6.6159(-02)	-6.6321(-02)	-6.5628(-02)	-6.6175(-02)	–
300×300	-6.7643(-02)	-6.7506(-02)	-6.8296(-02)	-6.7693(-02)	–
400×400	-6.7389(-02)	-6.7508(-02)	-6.7438(-02)	-6.7521(-02)	–
124×124	–	–	–	–	-6.8160(-02)

Table 3 Damping rate of the leading mode of the square lid-driven cavity at $Re = 100$ obtained using linear instability analysis. In all cases the frequency of the leading mode is equal to zero. $a.b(c) = a.b \times 10^c$.

$N_x \times N_y$	Model III (SRT)	Model III (MRT)	Model IV (SRT)	Model IV (MRT)	Semtex
100×100	-5.4040(-01)	-5.4040(-01)	-5.4047(-01)	-5.4048(-01)	–
124×124	–	–	–	–	-5.4131(-01)

Table 4 Damping rate of the leading mode of the square lid-driven cavity at $Re = 1000$ obtained using linear instability analysis. In all cases the frequency of the leading mode is equal to zero. $a.b(c) = a.b \times 10^c$.

$N_x \times N_y$	Model III (SRT)	Model III (MRT)	Model IV (SRT)	Model IV (MRT)	Semtex
200×200	-6.5536(-02)	-6.7115(-02)	-6.6288(-02)	-6.6271(-02)	–
300×300	-6.6918(-02)	-6.7648(-02)	-6.7283(-02)	-6.7273(-02)	–
400×400	–	-6.7834(-02)	–	-6.7625(-02)	–
124×124	–	–	–	–	-6.8160(-02)

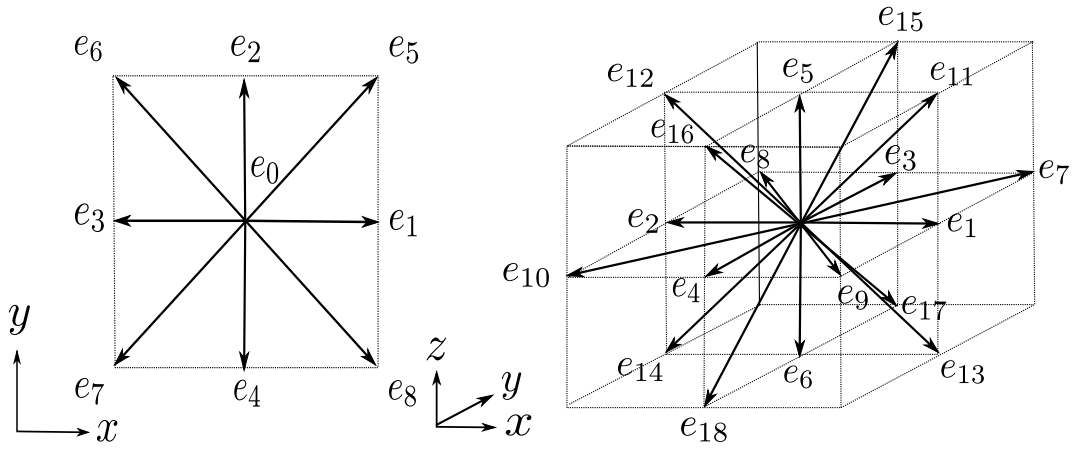

Fig. 1 Molecules D2Q09 (*left*) and D3Q19 (*right*)

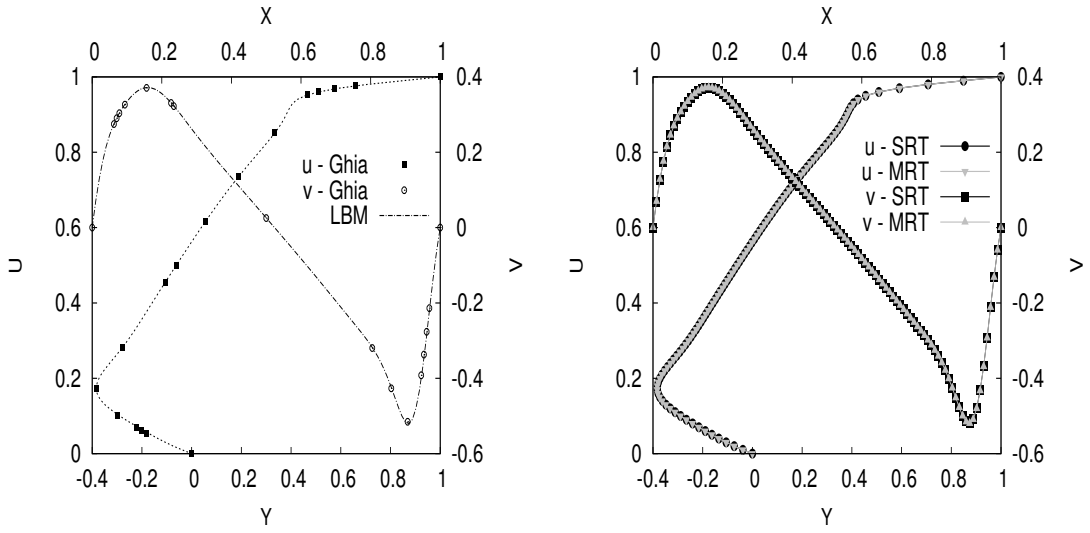

Fig. 2 Validation of the two-dimensional LBM base flow at $Re = 1000$. (*Left*): u−velocity along vertical center-line and v−velocity along horizontal center-line for single lid-driven square-cavity at Re=1000 using the standard model with SRT are compared with Ghia *et al.*[22] (*Right*): The same comparison for the velocity profiles using SRT and MRT models.

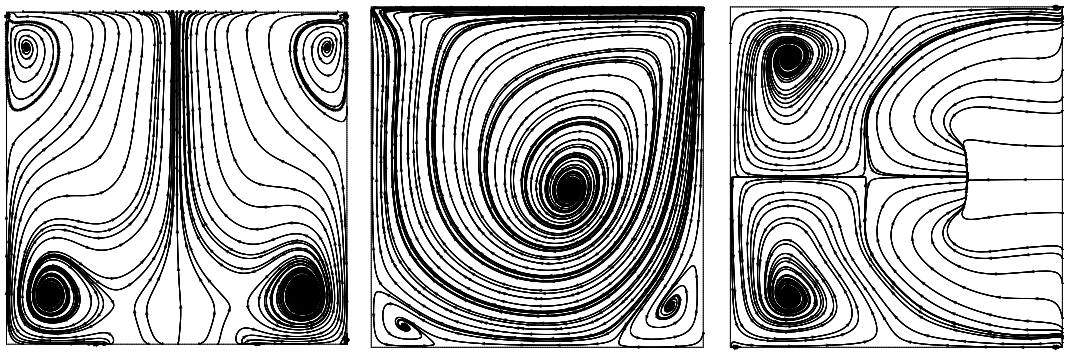

Fig. 3 Streamlines of the cubic lid-driven cavity at $Re = 1000$ at the center-planes.

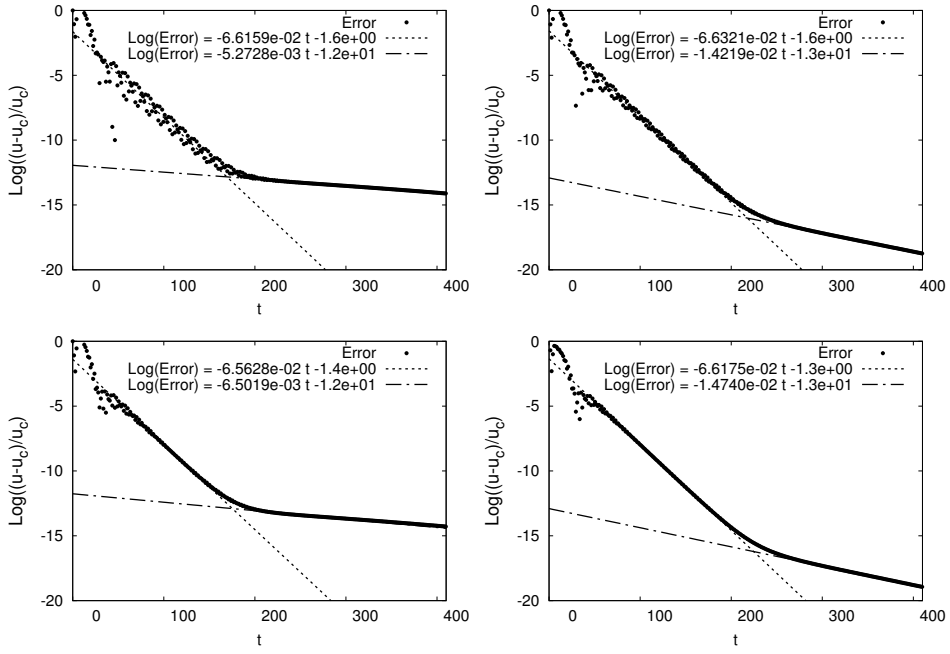

Fig. 4 Residual in the square lid-driven cavity flow at Reynolds 1000 obtained using the LBM (models III (*up*) and IV (*down*)). (*Left:*) SRT. (*Right:*) MRT.

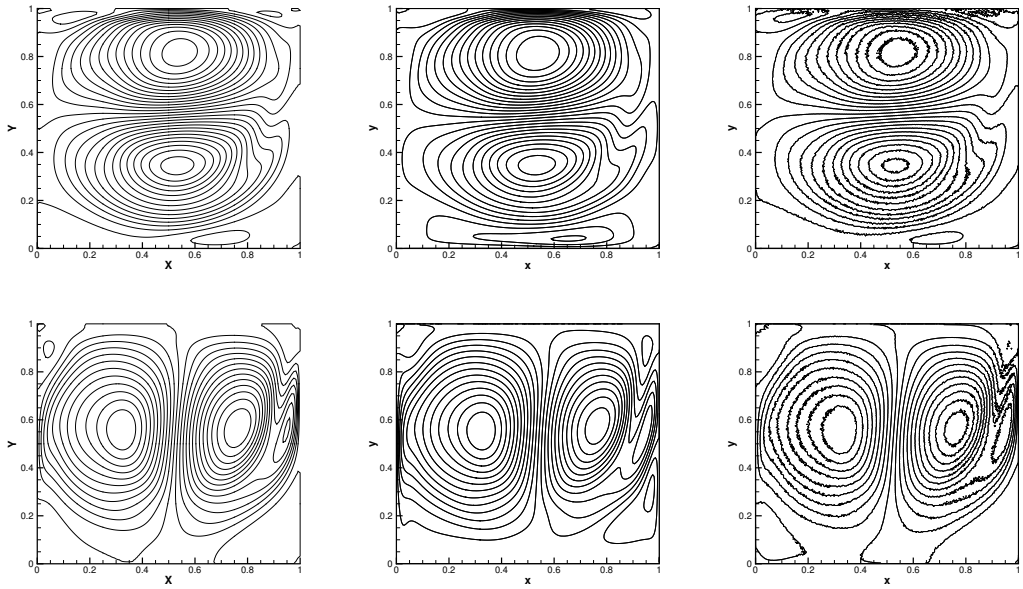

Fig. 5 Square lid-driven cavity. $\hat{u}$ (*upper row*) and $\hat{v}$ (*lower row*) amplitude functions of the leading mode at $Re = 1000$. *Left column:* Spectral code, *center column:* LBM-SRT, *right column:* LBM-MRT

Table 5 Leading eigenvalue of the cubic lid-driven cavity at $Re = 200$ obtained by linear instability analysis, and comparison with the result provided by Gómez et al [20].

Model	$N_x \times N_y \times N_Z$	Leading eigenvalue
Model III (SRT)	$100 \times 100 \times 100$	-0.415 $\pm$ 0.137 i
Model IV (SRT)	$100 \times 100 \times 100$	-0.416 $\pm$ 0.137 i
Gomez et al.	$96 \times 96 \times 96$	-0.403 $\pm$ 0.132 i

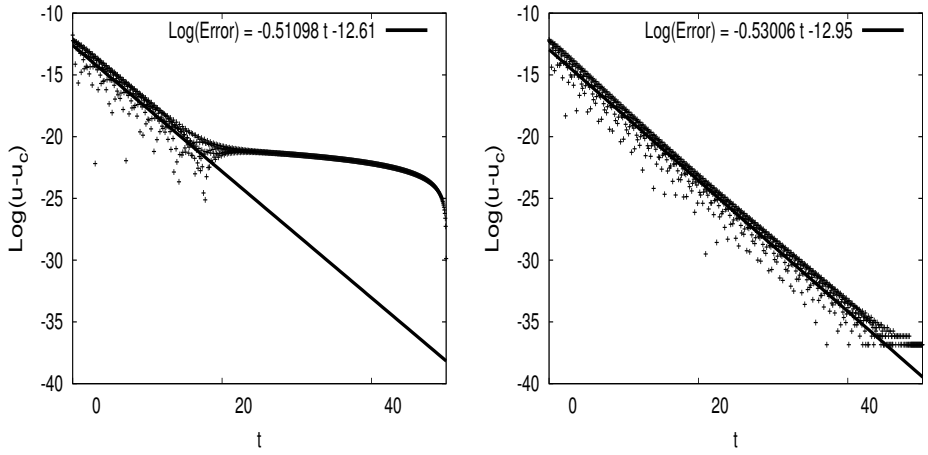

Fig. 6 Residual in the cubic lid-driven cavity flow at Reynolds 100 obtained using the linearized version of the LBM (models III and IV) starting from the steady base flow plus a random perturbation. *Left:* Model III (with SRT). *Right:* Model IV (with MRT).

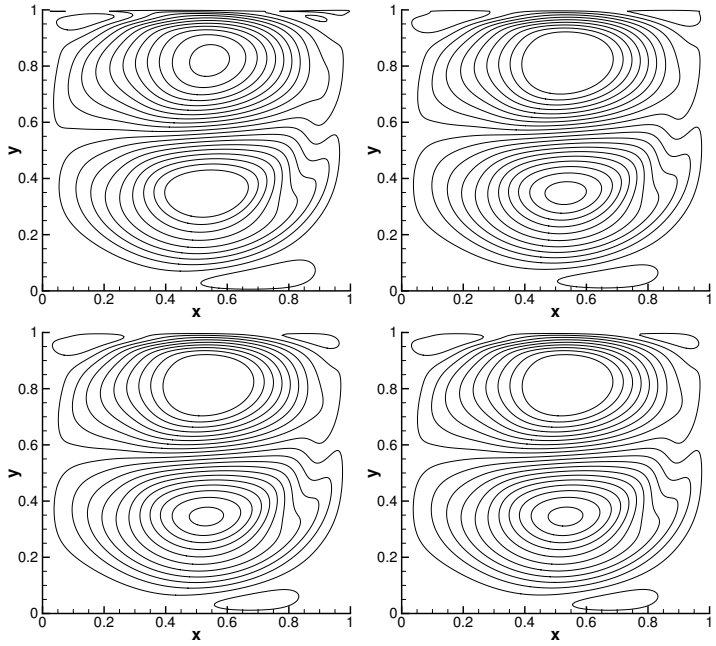

Fig. 7 Square lid-driven cavity. $\hat{u}$ amplitude function of the leading mode at $Re = 1000$ using the linearized version of the LBM (models III (up) and IV (down)). (*Left:*) SRT, (*Right:*) MRT. Resolution $N_x \times N_y = 200 \times 200$.

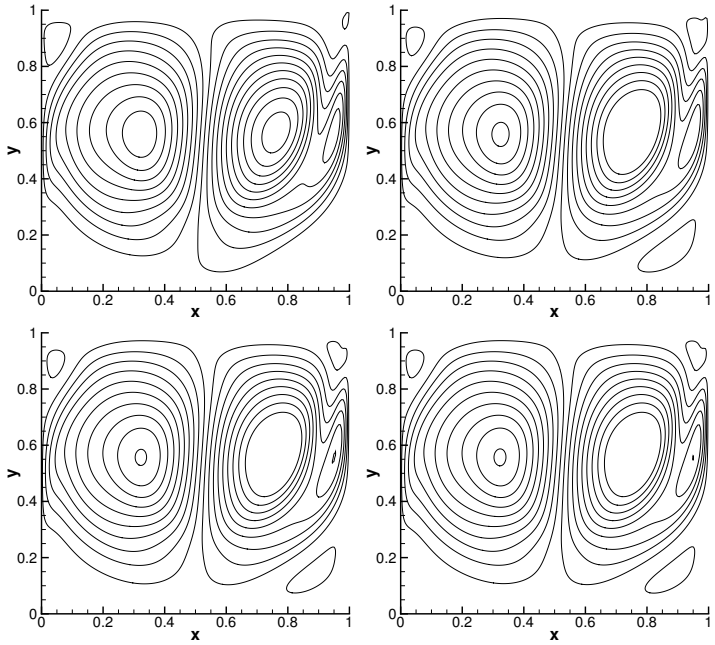

Fig. 8 Square lid-driven cavity. $\hat{v}$ amplitude function of the leading mode at $Re = 1000$ using the linearized version of the LBM (models III (up) and IV (down)). (*Left:*) SRT, (*Right:*) MRT. Resolution $N_x \times N_y = 200 \times 200$.

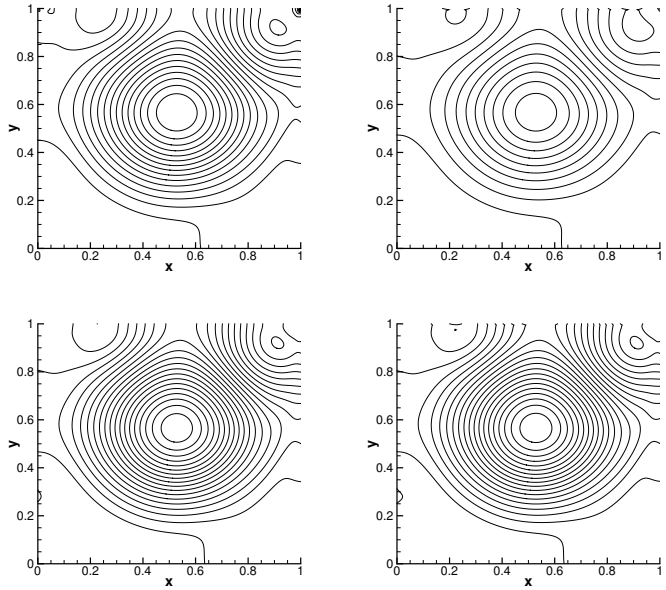

Fig. 9 Square lid-driven cavity. $\hat{p}$ amplitude function of the leading mode at $Re = 1000$ using the linearized version of the LBM (models III (up) and IV (down)). (*Left:*) SRT, (*Right:*) MRT. Resolution $N_x \times N_y = 200 \times 200$.

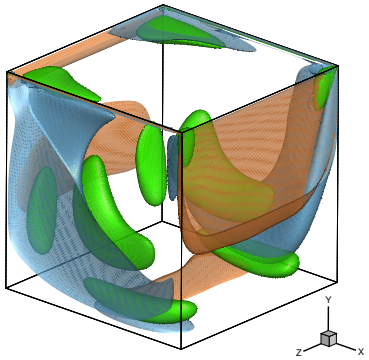

Fig. 10 Cubic lid-driven cavity. Leading mode at $Re = 1000$: (*blue*) $\hat{\omega}_x$, (*red*) $\hat{\omega}_z$ and (*green*) $\hat{w}$.

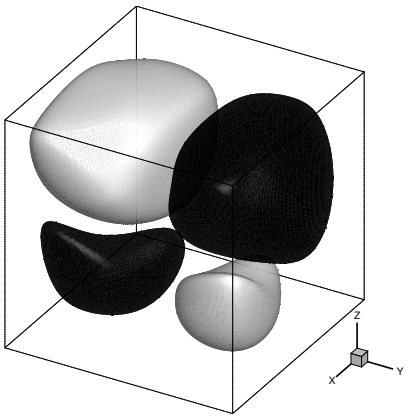

Fig. 11 Real part of the amplitude function $\hat{u}$ of the leading mode of the cubic lid-driven cavity at $Re = 200$. Resolution $N_x \times N_y \times N_z = 100$.

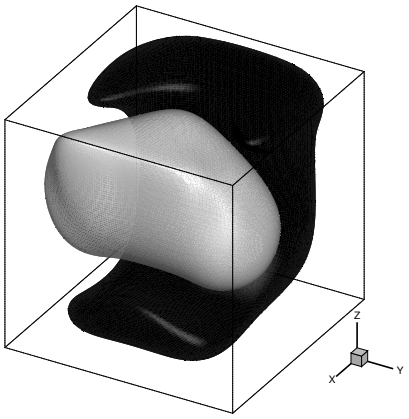

Fig. 12 Real part of the amplitude function $\hat{v}$ of the leading mode of the cubic lid-driven cavity at $Re = 200$. Resolution $N_x \times N_y \times N_z = 100$.

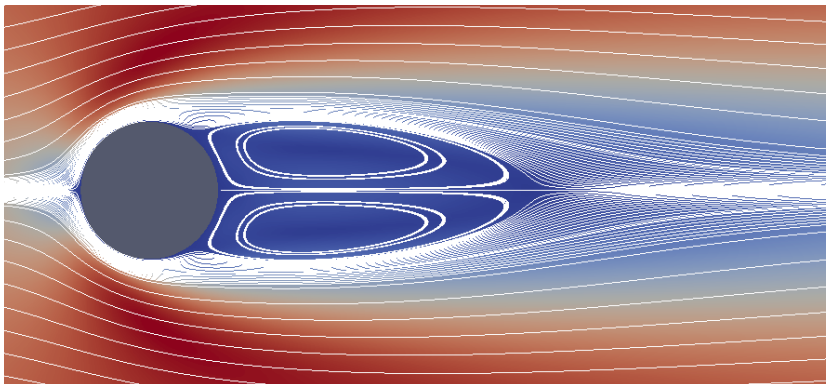

Fig. 13 Streamlines of base flow around a circular cylinder at $Re = 40$.

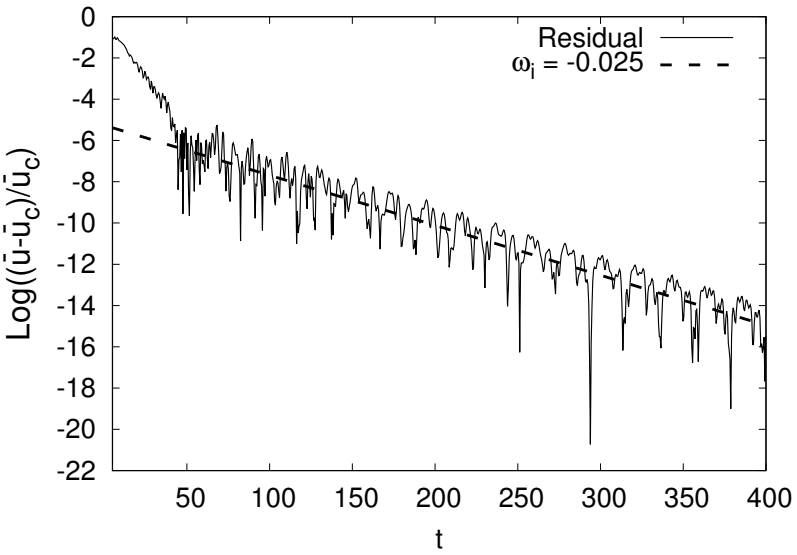

Fig. 14 Residual in the flow around a circular cylinder at $Re = 40$ using the LBM. $\overline{u}$ is the streamwise velocity component at position $(15, 11)$ and $\overline{u}_c$ is the corresponding converged value, [48].